

## Influence of the cerium-doped Fe<sub>2</sub>O<sub>3</sub> on structural and morphological properties for enhanced photocatalytic performance

G. T. Umamaheswari<sup>a,\*</sup>, N. Surumbarkuzhali<sup>b</sup>, K. Kulathuraan<sup>c</sup>, S. Subramani<sup>d</sup>, R. Thangarasu<sup>e</sup>, S. Arunachalam<sup>f</sup>, M. Kumar<sup>g</sup>

<sup>a</sup>*Department of Physics, Arignar Anna Government Arts College, Attur, Salem-636121, Tamilnadu, India*

<sup>b</sup>*Department of Physics, Government Arts College, Salem – 636007, Tamilnadu, India*

<sup>c</sup>*Department of Physics, Arulmigu Palaniandavar College of Arts & Culture, Dindigul Road, Palani-624601*

<sup>d</sup>*Department of Electronics, PSG College of Arts & Science, Coimbatore- 641014, Tamilnadu, India*

<sup>e</sup>*Department of Physics, K.S. Rangasamy College of Arts & Science, Tiruchengode-637215, Tamilnadu, India*

<sup>f</sup>*Department of Electrochemistry, Saveetha School of Engineering (SIMATS), Thandalam, Chennai-602105, Tamilnadu, India.*

<sup>g</sup>*Department of Environmental Engineering and Management, Chaoyang University of Technology, Taichung City - 413310, Taiwan*

In this study, pure and Ce-doped Fe<sub>2</sub>O<sub>3</sub> nanoparticles were prepared using the sol-gel technique, and the microstructural, morphological, electrical, and photocatalytic activities were studied. Here, these prepared samples were characterized by XRD, FTIR, HR-TEM, and SEM) with EDAX. The XRD pattern demonstrates that the Fe<sub>2</sub>O<sub>3</sub> nanorods are highly crystalline, and Ce ions were properly incorporated into the Fe<sub>2</sub>O<sub>3</sub> lattice. SEM images are to facilitate increasing Ce doping, nanorods, and nanosphere-like structures smooth Fe<sub>2</sub>O<sub>3</sub> nanorods have appeared. The lattice spacing growth with SAED pattern along the direction plane [018] was measured to be roughly 0.21 nm, and element mapping using EDX analysis is observed to the distribution of Fe, Ce & O elements. The functional groups and chemical interactions of Ce-substituted Fe<sub>2</sub>O<sub>3</sub> samples were measured using FTIR spectroscopy. In particular, a novel photocatalytic activity of the products was considered using methylene blue. The findings suggest that Ce-doped Fe<sub>2</sub>O<sub>3</sub> products have greater MB reduction efficiency than undoped Fe<sub>2</sub>O<sub>3</sub>.

(Received March 7, 2022; Accepted October 8, 2022)

*Keywords:* Structural, Morphological, Electrical, Cerium, Photocatalytic activity

### 1. Introduction

During the past years, environmental problems, exclusively the water pollution which is caused by the discharge from dye industries of organic chemistry and costume textile corporation have provided the stimulus for the applied research in the area of eco-friendly remediation [1]. The imperative sites are the improvement of the science arena and technology by manipulators in various fields with distinctive properties [2]. Nano-iron oxide is frequently utilized in power facilities due to its excellent concealment ability, color strength, and chemical stability [3]. Iron oxide, with distinct enriched phases, is Fe in varying oxidation states depending on the reduction process of the phases. Iron oxide includes hematite ( $\alpha$ -Fe<sub>2</sub>O<sub>3</sub>), magnetite (Fe<sub>3</sub>O<sub>4</sub>), and wustite (FeO). The Fe<sub>2</sub>O<sub>3</sub> exhibits several polymorphs with  $\alpha$ -Fe<sub>2</sub>O<sub>3</sub> (rhombohedral),  $\gamma$ -Fe<sub>2</sub>O<sub>3</sub> (cubic),  $\beta$ -Fe<sub>2</sub>O<sub>3</sub> (cubic), and  $\varepsilon$ -Fe<sub>2</sub>O<sub>3</sub> (orthorhombic). Therefore, the-Fe<sub>2</sub>O<sub>3</sub> is the most stable phase thermodynamical. The iron oxide (Fe<sub>2</sub>O<sub>3</sub>) crystalline structures were  $\alpha$ ,  $\beta$  &  $\gamma$  as well-known

\* Corresponding author: gtumamakeshwari21@gmail.com  
<https://doi.org/10.15251/DJNB.2022.174.1135>

semiconductor materials with narrow band gap energy between 1.9 and 2.2 eV [4-5]. The introduction of impurity ions into the Fe<sub>2</sub>O<sub>3</sub> host matrix structures are magical and effective process to develop unique functionalities thereby Fe<sub>2</sub>O<sub>3</sub>. For example, dilute doping of lanthanide series elements are inner-transition metal ions (e.g. Ny<sup>+3</sup>, Sm<sup>3+</sup>, Gd<sup>+3</sup> & Ce<sup>4+</sup>) incorporation into the magnetic Fe<sub>2</sub>O<sub>3</sub> system can introduce ferri-magnetic functions though its magnetic properties can be reminisced [6]. Among non-transition metals, Ce<sup>4+</sup> and Fe<sup>3+</sup> have been found to be the most favorable elements; thereby, the optical and magnetic properties of Fe<sub>2</sub>O<sub>3</sub> have been reported [7]. Theoretically, with different lanthanide metals (LM= Sm, Ny, Ce, Gd, Er, Pm & Yb etc). Hematite structure ( $\beta$ - Fe<sub>2</sub>O<sub>3</sub>), which is the most stable form of iron oxide, is an n-type magnetic photocatalyst in environmental applications because of the good band gap and simple manufacturing into the magnetic property [8]. Combination materials, such as binary and ternary nanostructures, can improve photocatalytic activity by transferring photogenerated electrons from the conduction band (CB) of one semiconductor with a higher band to another with a lower CB thus improving visible light harvesting. In actuality, the photocatalyst should have an appropriate band gap, chemical stability, and efficient charge carrier separation [9–10]. Nanostructured metal oxides, including TiO<sub>2</sub> [11], Fe<sub>2</sub>O<sub>3</sub> [12-13], CeO<sub>2</sub> [14], ZnO [15], MnO<sub>2</sub>[16], Fe<sub>3</sub>O<sub>4</sub>[17], SnO<sub>2</sub>[18] and Cu<sub>2</sub>O [19] have been applied to derive chemical reactions with solar energy instead of tradition energies due to their economic and technical feasibility. It has also been demonstrated that their photocatalytic activity could be largely enhanced by using synthetic nanomaterials. As Fe<sub>2</sub>O<sub>3</sub> photocatalysts, magnetic characteristics of the materials should be determined using the following standards: (1) High photocatalytic activity and (2) affordability (3) high yield, as a large amount of materials is required. Many solution-based sol-gel approaches have been described for broadly regulating the microstructure, lattice plane, and chemical bonding nature with the goal of tuning the performance of the Fe<sub>2</sub>O<sub>3</sub> magnetic materials, given the substantial dependency on performance. By tuning the size and morphology, the photocatalytic activity of tailored by adjusting dopants and doping concentration of the ceria. Inserting the transition metal ions into the iron oxide crystal lattice triggered the improvement of bandgap, magnetic, electrical, and optical properties of Fe<sub>2</sub>O<sub>3</sub>, which is due to the very fast recombination of photogenerated electron-hole pairs. It has been suggested that doping certain cations, which can perform as electron-trapping agents to reduce the electron-hole recombination rate, might increase the photocatalytic performance of magnetic photocatalysts [20–21]. The diverse features of the Ce-doped Fe<sub>2</sub>O<sub>3</sub> nanoparticles have drawn much interest in investigating potential applications in various technologies. Ce-doped Fe<sub>2</sub>O<sub>3</sub> nanostructures have been researched and proposed for dye degradation [22]. Consequently, in this work, we constructed Ce doped Fe<sub>2</sub>O<sub>3</sub> heterojunction photocatalyst via the sol-gel method strategy in order to degrade of dye aqueous solution, which was methylene blue (MB). Furthermore, the physicochemical properties of the resulting Ce-doped Fe<sub>2</sub>O<sub>3</sub> heterojunction were studied through XRD, TEM, SEM with EDAX, and FTIR. Moreover, the photocatalytic performance mechanism of Ce-doped Fe<sub>2</sub>O<sub>3</sub> heterojunction was proposed reasonably.

## **2. Materials and experimental procedure**

### **2.1. Materials**

Ferric chloride hexahydrate (FeCl<sub>3</sub>.6H<sub>2</sub>O) powder (ZAD, Merck, 99%), Oxalic acid C<sub>2</sub>H<sub>2</sub>O<sub>4</sub>.2H<sub>2</sub>O (OXL, Merck, 90.0%), Ethanol (AR 99.9%) and Cerium chloride anhydrous (CeCl<sub>3</sub>.7H<sub>2</sub>O) (MAD, Merck, 99.9%), are used for the prepared the Fe<sub>2</sub>O<sub>3</sub> nanoparticles. Other chemicals used are of reagent grade. Deionized (D.I) water is used throughout the experiment and the purchased chemicals are used without any additional purification.

### **2.2. Experimental procedure**

The typical synthesis process consists of two steps. Step I: The required amount of Ferric chloride hexahydrate (FeCl<sub>3</sub>.6H<sub>2</sub>O) (2.195g) was dissolved in 20 ml of Ethanol. This mixture was kept under Vigorous stirring for about 30 minutes till a homogenous solution was obtained. Then 1.2607g of Then, a small amount of Oxalic acid (C<sub>2</sub>H<sub>2</sub>O<sub>4</sub>.2H<sub>2</sub>O) (0.05 g) was added as a capping

agent in the reaction system and stirred well at 40-50°C using a magnetic hot plate for 24 h. After completion of the process, the solution was allowed to get settled light brown yields. Both the solutions were put together into a stainless-steel autoclave with a Teflon liner and sealed. Then it was kept at 80°C for 5 hours. Then the precipitate is formed, which is washed by de-ionized water repeatedly and dried for about 60°C for 1 hour using a muffle furnace. The product was ground to fine powder creation and was allowed to attain room temperature at a cooling rate of 5°C/min to obtain the brown-colored Fe<sub>2</sub>O<sub>3</sub> nanoparticles.

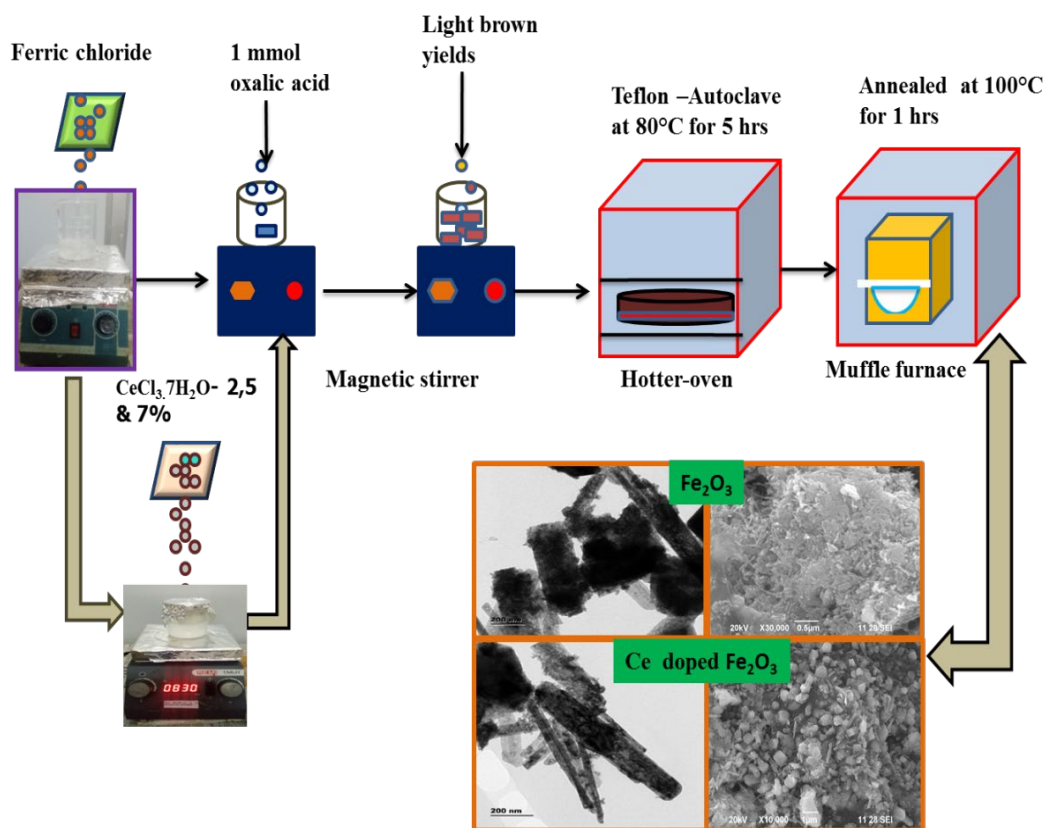


Fig. 1. Experimental process of pure Fe<sub>2</sub>O<sub>3</sub> and Ce doped Fe<sub>2</sub>O<sub>3</sub> nanoparticles by Sol-Gel method.

Step II: For the synthesis of Ce-doped Fe<sub>2</sub>O<sub>3</sub> (Ce: Fe<sub>2</sub>O<sub>3</sub>; where 2, 5 and 7%), an estimated amount of cerium nitrate (x) was mixed with aqueous ferric chloride solution. Furthermore, the needed amount of oxalic acid was added dropwise into the homogeneous mixture to get a dark brown color. After achieving a dark brown color, the same approach as in Step I was used to create the Ce-doped Fe<sub>2</sub>O<sub>3</sub> nanoparticles, and Figure 1 depicts an overview of the synthesis stages.

### 2.3. Characterization Techniques

The elaborated Fe<sub>2</sub>O<sub>3</sub> and Ce: Fe<sub>2</sub>O<sub>3</sub> layers were investigated for their microstructural and morphological properties. X-ray “SHIMADZU” diffractometer was used to study the crystallinity in the range of 20-80° under the step size 0.02° with CuKα (λ = 1.54 Å). From XRD patterns, we can appreciate the crystalline phase and structure. The micro and nano-surface morphologies of the products were examined by high-resolution transmission electron microscopy (TECHNAI T20). The surface morphologies were observed through a scanning electron microscopy (JOEL JSM 6390). The elemental composition was investigated using EDAX (energy dispersive X-ray analysis (TINCA PENTEL FET X3 EDAX instrument from OXFORD)). The chemical nature of the bonds as-prepared sample was confirmed by a Fourier-transform microscopic infrared spectrometer (BRUKER IFS 66V FTIR).

## 2.4. Photocatalytic activity

The model dye chemical was methyl blue (MB), which was of analytical grade. Under UV light irradiation, MB was degraded in the presence of non-transition metal-doped nanoparticles. In 100 mL of an aqueous solution of MB, a constant starting concentration of 40 mg/L of nanoparticles serving as a photocatalyst was added. The suspensions were sonicated for 30 minutes in the dark before being exposed to radiation to create a colloidal solution. In each experiment, 40 mg of the photocatalyst was suspended in 40 mL of 25 mg/L MB aqueous solution in a beaker. The mixed solution was magnetically stirred for 30 minutes at the adsorption/desorption equilibrium before illumination. Every hour, a 4mL sample of the solution was obtained, centrifuged, and the supernatant removed in order to assess the UV-vis absorption. Using a UV-Vis spectrophotometer with the model number (UC-2450-SHIMADZU), the absorption spectra were recorded at the maximum characteristic absorption wavelength ( $\lambda_{\text{max}}$ ) nm. The intensity of the primary absorption peak (662) nm of the MB dye was referred to as a measure of the residual dye concentration. The photocatalytic degradation (PD) was determined by the following relation (1)

$$PD = \left[ \frac{C_o - C_t}{C_o} \right] \times 100\% \quad (1)$$

where  $C_o$  is the initial concentration of the solution which reached absorbency balance and  $C_t$  is the concentration of the dye solution at the irradiation time (t).

## 3. Results and discussion

### 3.1. XRD Analysis

The XRD diffraction patterns of the synthesized  $\text{Fe}_2\text{O}_3$  with various Ce 2, 5 & 7% concentrations are shown in Figures 2 (a-d). In these XRD spectra, the strong and sharp preferential orientation peak along the (008) plane at  $2\theta = 31.55^\circ$  which confirms the hexagonal structure of  $\text{Fe}_2\text{O}_3$ . The obtained diffraction peaks at  $2\theta$  are about,  $31.55^\circ$ ,  $34.17^\circ$ ,  $36.45^\circ$ ,  $47.34^\circ$ ,  $56.30^\circ$ ,  $62.53^\circ$ ,  $67.39^\circ$ ,  $68.97^\circ$  with the corresponding to the (hkl) planes of (0 0 8), (1 1 3), (0 1 8), (0 2 7), (2 1 6), (3 0 6), (2 2 0) and (2 1 11) respectively. All the diffraction peaks in (Fig. 2 a) are coincided well with standard JCPDS card no.76-1821 ( $a=5.560$ ,  $c=22.550 \text{ \AA}$ ), indexing to hexagonal  $\text{Fe}_2\text{O}_3$  phase, and no other secondary phases are noticed because of the purity of the samples is high. Figure 2b illustrates a shift in the position of the main peaks (008) to the higher side  $2\theta$  values for doped samples. This shift in the peak can be attributed to the ionic radii of the dopant ( $\text{Ce}^{4+}=1.01 \text{ \AA}$ ), which is smaller than that of the ionic radius of Fe ions ( $\text{Fe}^{3+}=0.64 \text{ \AA}$ ). The XRD lines with the shifting of the plane (008) doped  $\text{Fe}_2\text{O}_3$  suggest that  $\text{Ce}^{4+}$  content can be efficiently substituted to the  $\text{Fe}_2\text{O}_3$  host structure on the Ce spot. Apart from the shifting, the peak position is also found to be broadened in the concentration of  $\text{Ce}^{4+}$  in  $\text{Fe}_2\text{O}_3$ . This is attributed to the reduction of grain size and strain in the  $\text{Fe}_2\text{O}_3$  lattice with the incorporation of  $\text{Ce}^{4+}$  atoms, as shown in Fig 2 b. The grain size and microstrain of the pure and  $\text{Ce}^{4+}$  samples are estimated from the broadening of the diffraction peaks using the Debye –Scherrer formula [23] (2):

$$D = \frac{K\lambda}{\beta \cos \theta} \quad (2)$$

where  $D$ ,  $K$  (0.98),  $\lambda$ ,  $\beta$ , and  $\theta$  are denoted the crystallite size, shape factor, wavelength of the source, FWHM, and diffraction angle. The prepared materials micro-strain is determined by the following equation (3):

$$\varepsilon = \frac{\beta \cos \theta}{4} \quad (3)$$

where ' $\beta$ ' is the FWHM and  $\theta$  is the diffraction angle. The (008) plane is preferred to evaluate the crystalline size.

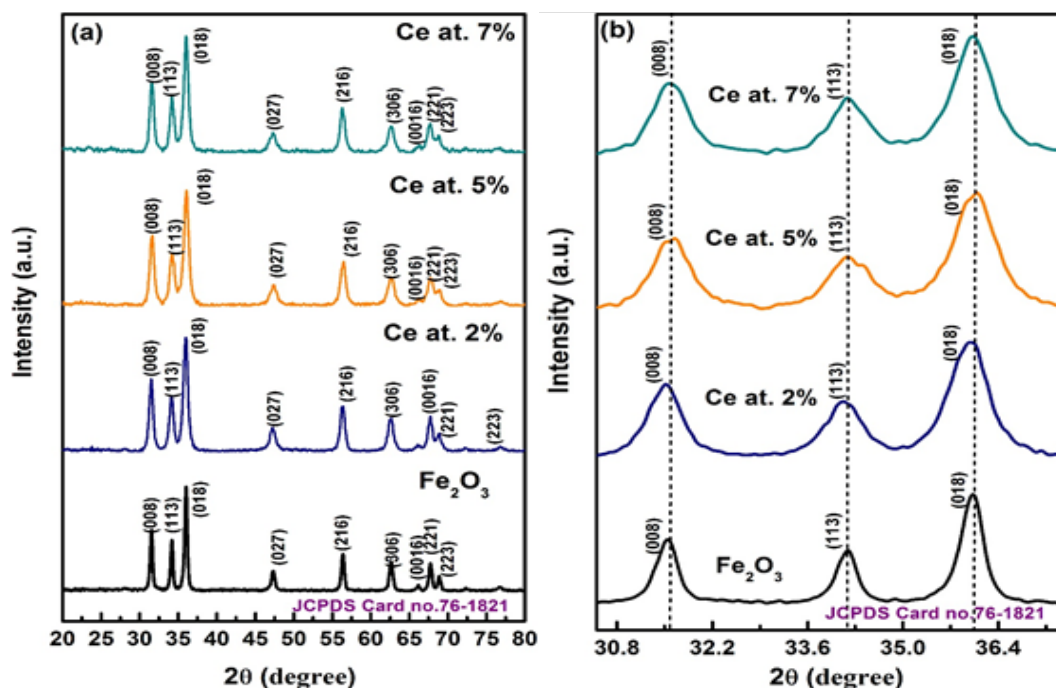


Fig. 2. (a, b) XRD patterns of (a)  $\text{Fe}_2\text{O}_3$  and Ce doped  $\text{Fe}_2\text{O}_3$  (b) a shift position of Ce doped  $\text{Fe}_2\text{O}_3$  nanostructure.

The crystalline size decreases, and the micro-strain value increases with the increase in the concentration of Ce at 2, 5 & 7%. The obtained results are listed in Table 1. The distortion of  $\text{Fe}_2\text{O}_3$  and content impurities of ( $\text{Ce}^{4+}$ ) are responsible for the decrease in nucleation and subsequent growth rate of  $\text{Fe}_2\text{O}_3$  NPs.

Table 1. The microstructural characteristics of pure and Ce-doped  $\text{Fe}_2\text{O}_3$  nanostructure.

$\text{Fe}_2\text{O}_3$ with Ce doped $\text{Fe}_2\text{O}_3$	$2(\theta)$ degree	(h k l)	FWHM	Grain size (D)nm	Microstrain ( $\epsilon$ ) $10^4 \text{lin}^{-2} \text{m}^2$	Dislocation density ( $10^{14}$ lines/ $\text{m}^2$ )
0	31.5581	(008)	8.4614	10.19	0.035529	9.6307
	34.1724	(113)	0.3064	28.33	0.012781	1.2459
	35.9159	(018)	0.3443	25.34	0.001429	1.5573
2	31.5798	(008)	1.3988	61.64	0.005873	2.6317
	33.9831	(113)	0.4629	18.74	0.001932	2.8466
	35.9495	(018)	0.5632	15.48	0.002338	4.1687
5	31.5798	(008)	1.9943	43.23	0.008374	5.3495
	34.2016	(113)	0.6455	13.44	0.002692	5.5289
	36.1680	(018)	0.6093	14.32	0.002527	4.8735
7	31.5126	(008)	0.5488	15.70	0.002305	4.0522
	34.1344	(113)	0.5708	15.20	0.002381	4.3249
	35.8823	(018)	0.6245	13.96	0.002592	5.1273

The increase in the microstrain shows the enhancement in the concentration of the lattice imperfections which is the quality of the samples. As shown in Fig. 2 d, the dislocation density of

the crystals structure for preferential (hkl) orientation values are determined using the following relation (4)

$$\delta = \frac{1}{D} \quad (4)$$

The dislocation density samples changed by an increase in doping content are listed in Table 1. A small dislocation density is an indication of good crystallization of the NPs. Hence, the conclusion provides evidence of the effect of Ce-doped  $\text{Fe}_2\text{O}_3$  NPs. Three concentrations of cerium (2, 5, and 7 weight percent) were employed as dopants to study how the cerium content doped into  $\text{Fe}_2\text{O}_3$  impacts the associated characteristics. With increasing cerium concentration, it is observed that the intensity of the significant diffraction peaks grows and that the peak's position shifts a little towards a lower angle, indicating that cerium doping increased the lattice parameters and decreased the crystalline quality and size of  $\text{Fe}_2\text{O}_3$ . The crystallinity of  $\text{Fe}_2\text{O}_3$  nanoparticles deteriorates as a result of cerium doping. The size of the crystallites in their investigations reduces as a consequence of the inhibition of the development of the nanoparticles caused by the presence of some cerium during the doping process, which may be present in or close to the boundary of the  $\text{Fe}_2\text{O}_3$  nanoparticles.

### 3.2 TEM Study

Transmission electron microscopy (TEM) was used to determine the  $\text{Fe}_2\text{O}_3$  and Ce-doped  $\text{Fe}_2\text{O}_3$  material morphology. Fig. 3(a-d) shows the TEM image of pure  $\text{Fe}_2\text{O}_3$  composed of small tightly-packed two-dimensional bundle nanorods. The HRTEM image of  $\text{Fe}_2\text{O}_3$  nanorods in Fig. 3a shows the well-resolved lattice spacing of 0.216 nm matching to d-spacing and is related to (018) plane hexagonal  $\text{Fe}_2\text{O}_3$ . Fig 3 b, c, d presents the bright field TEM images of  $\text{Fe}_2\text{O}_3$  and Ce-doped  $\text{Fe}_2\text{O}_3$ . The presence of images is merged nanorods and nanoneedle particles with less agglomeration by TEM images.

The diameter and the length of 2% Ce doped  $\text{Fe}_2\text{O}_3$  nanorods. The TEM image of Figure 3c represents the average diameter and length of 5% Ce-doped  $\text{Fe}_2\text{O}_3$  nanorods measured as 0.75 and 1.7  $\mu\text{m}$ , respectively.

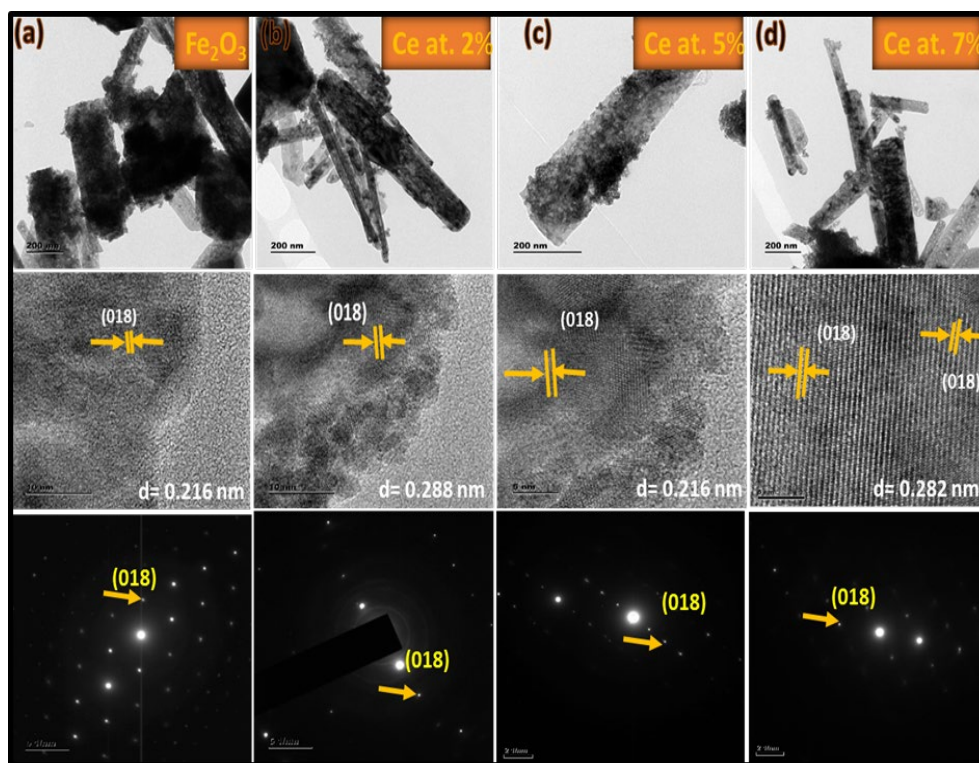


Fig. 3. HRTEM images of (a)  $\text{Fe}_2\text{O}_3$  (b) Ce at.2% (c) Ce at. 5% & (d) Ce at.7% Ce doped  $\text{Fe}_2\text{O}_3$  nanostructure.

The measured value indicates a slight increment in dimensions, and many nanorods show a rough surface with a needle shape. The uniform and straight nanorods with a diameter of 406 nm and length of 845 nm are obtained at 7% Ce doping in  $\text{Fe}_2\text{O}_3$  [24]. The decrease in the average length and diameter of Ce-doped  $\text{Fe}_2\text{O}_3$  nanorods may denote that the overall growth rate decrease in all dimensions is due to Ce doping and surfactant influence on Ce ions at growing planes and hindrance among the ferric species in growth. The lattice d-spacing of Ce doped  $\text{Fe}_2\text{O}_3$  nanorods is calculated from the HRTEM images, Fig. 3 b, c, d, is 0.288-0.216 nm, in agreement with a lattice spacing of (018) plane of  $\text{Fe}_2\text{O}_3$ . The SAED pattern assists the element that the prepared nanoparticles have a high degree of crystalline nature. The diffraction patterns are associated with the (018) plane of the hexagonal structure, and it is attributed to the short-range ordering among the unit cells caused by the doping, indicating the decreased the crystallinity of Ce-doped  $\text{Fe}_2\text{O}_3$  samples.

### 3.3. SEM-EDAX Analysis

SEM investigated the morphology of the typical  $\text{Fe}_2\text{O}_3$  and Ce-doped  $\text{Fe}_2\text{O}_3$  nanorods in Figure 4 a-d, where the samples with high-yield rod-like structures with plate, sheet, wire, and needle can be observed. Figure 4a presents the microstructures made up of the different types of structures that are agglomerated particles on the surface of  $\text{Fe}_2\text{O}_3$ . A change in morphology confirms the dopant substitution in the  $\text{Ce}^{2+}$  lattice due to the presence of different particles size (compact lumps, up to several microns) surrounding a loose atmosphere shown in Figure 4b-d. The morphology growth induced on pure and Ce-doped  $\text{Fe}_2\text{O}_3$  samples is shown in Figure 4 b-d. The images indicate the homogenous, well-shaped nanorods with a diameter of  $92 \pm 4$  nm and a length of  $650 \pm 40$  nm.

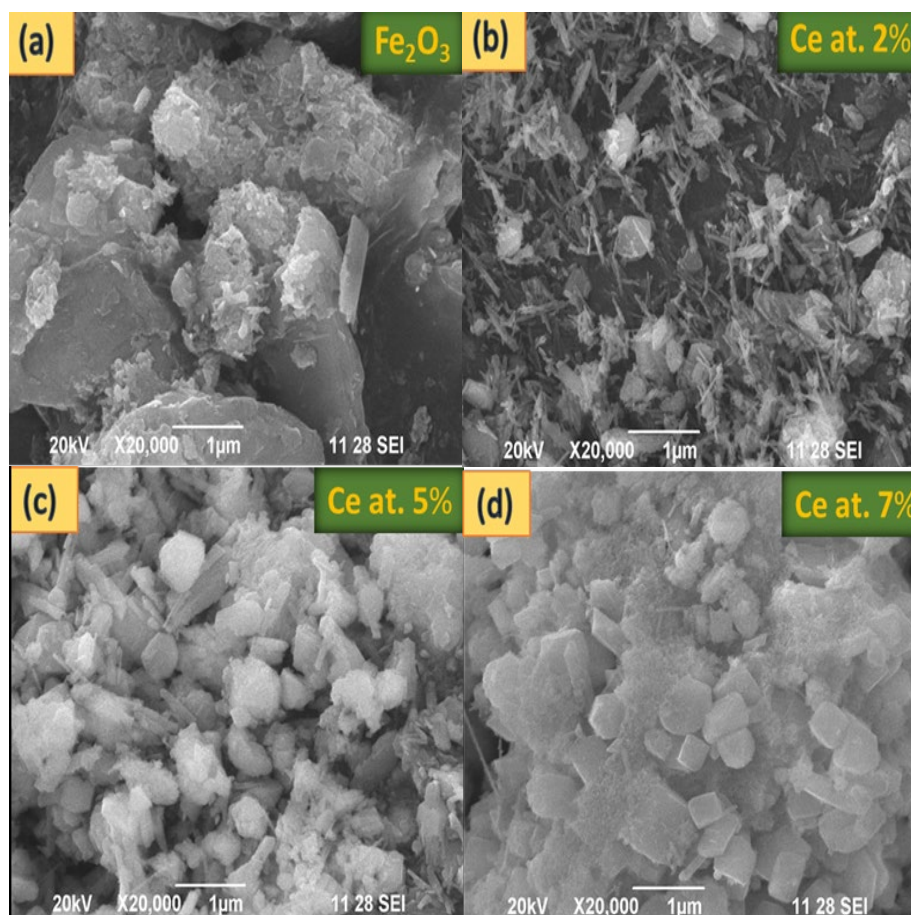


Fig. 4. (a-d) SEM micrograph Ce doped  $\text{Fe}_2\text{O}_3$  nanostructure a)  $\text{Fe}_2\text{O}_3$  b) Ce at.2% c) Ce at. 5% & d) Ce at.7% nanostructure.

Figure 4 c reports the formation of nanorods of undoped  $\text{Fe}_2\text{O}_3$  with various types of structures that resemble a hexagonal face. These suggest that the surface diffusion phenomenon plays an essential role in the thermal growth process of nanorods. Herein, the nanorods' dimension became smaller when the Ce doping concentration increased. These may be attributed to rapid growth along the (008) direction since the Ce doping can promote the growth of  $\text{Fe}_2\text{O}_3$  along the c axis. At 2% Ce doping, a more uniform plate, sphere-like with a small needle, is the smallest diameter found in large areas.

At 5% Ce doping, the considerable distortion influenced the normal development behavior of rods, spheres, octal, and small flowers, resulting in the formation of ball-like particles in addition to nanorods. The nanorod configurations are replaced by tightly linked disks, rods, octal, 4-conal, spheres, and plate-like particles at 7% Ce doping. As a result, morphological variation may be caused by dipolar interaction along the C-axis and the impact of  $\text{Ce}^{3+}$  ions on the  $\text{Fe}^{4+}$  site.

Energy dispersive spectroscopy (EDX) was used further to investigate the elemental composition of the pure and Ce-doped  $\text{Fe}_2\text{O}_3$  materials. The Fe, Ce, and O elements were effectively identified on the sample, as recorded EDX spectra are illustrated in Fig 5. (a-d). The elemental composition percentages are tabled in the inset Fig 5(a-d). Finally, these results confirm the pure and Ce-doped  $\text{Fe}_2\text{O}_3$  materials formation.

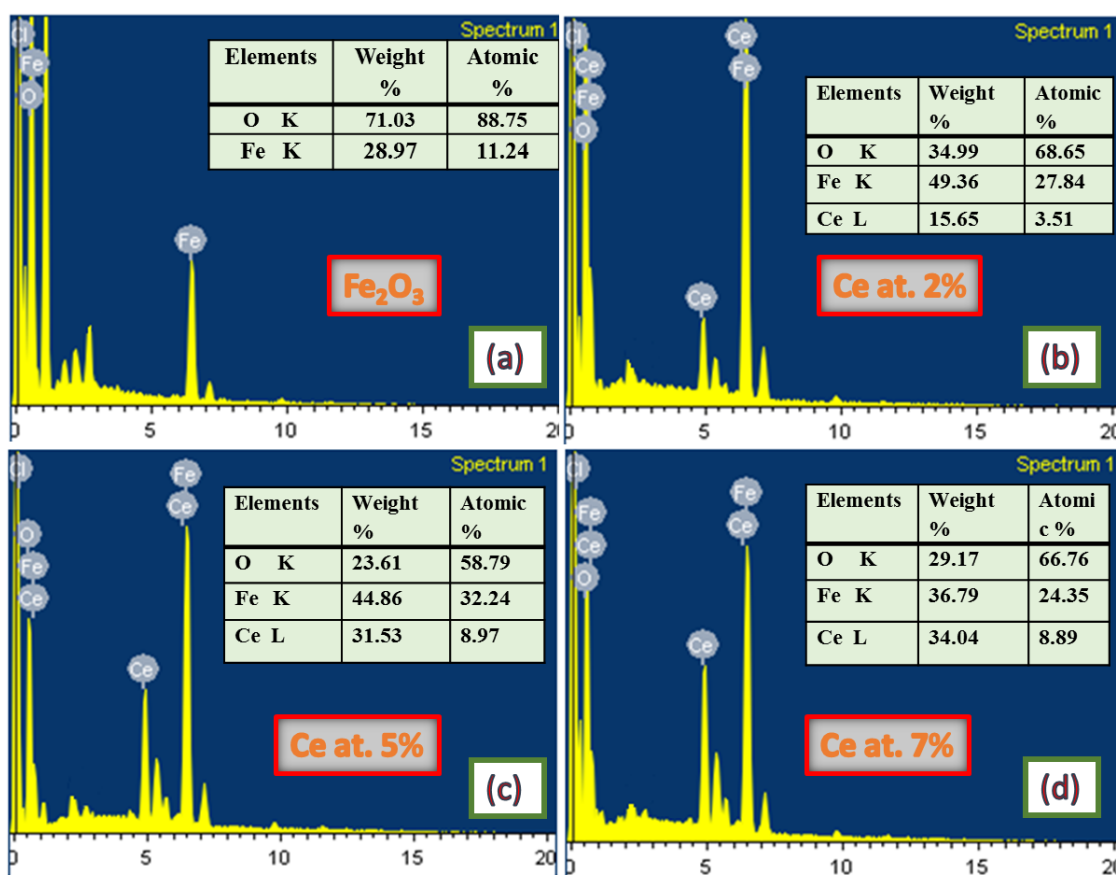


Fig. 5. EDAX spectrum of (a)  $\text{Fe}_2\text{O}_3$ , (b) Ce at. 2% (c) Ce at. 5% & (d) Ce at. 7% Ce doped  $\text{Fe}_2\text{O}_3$  nanostructure.

### 3.4. FTIR Study

The FTIR technique is used to categorize the molecular geometry with functional groups and the intra- or intermolecular interactions present in the samples [25]. The position and numbers of bands depend on the chemical element's composition and crystalline structure. The current work

investigated the vibrational modes of pure and Ce-doped  $\text{Fe}_2\text{O}_3$  nanoparticles using the FTIR technique.

Fig. 6 depicted the recorded FTIR spectra of pure and Ce-doped  $\text{Fe}_2\text{O}_3$  nanoparticles. From fig.6, the broadband between 3300 and 3600  $\text{cm}^{-1}$  is assigned to O-H stretching vibration modes [26]. At 3477  $\text{cm}^{-1}$ , a broad peak is detected, which is ascribed to the stretching mode of a hydroxyl group (O-H) present on the surface. A peak at 2320  $\text{cm}^{-1}$  is regarded as  $-\text{CH}_2-$  and  $-\text{CH}_3-$  groups. Two peaks detected at 1702 and 1459  $\text{cm}^{-1}$  are attributed to the carbonyl groups' asymmetric (C-O) and symmetric stretching (C-O) frequencies. The appearance at 462-566  $\text{cm}^{-1}$  is assigned to the vibration mode of Fe-O-Fe stretching, while weak peaks observed at 845  $\text{cm}^{-1}$  [27]. The position of the absorption band in Ce-doped  $\text{Fe}_2\text{O}_3$  samples is similar to those in the  $\text{Fe}_2\text{O}_3$  sample, which implies that layer structure is expressively altered by intercalation. Fig 6 that the infrared absorption bands appeared for Cerium doped  $\text{Fe}_2\text{O}_3$  at 5 &7% crystals are increasing band vibration at 2351  $\text{cm}^{-1}$ , 1545  $\text{cm}^{-1}$ , 1341  $\text{cm}^{-1}$ , 1045  $\text{cm}^{-1}$  and 523-444  $\text{cm}^{-1}$ .

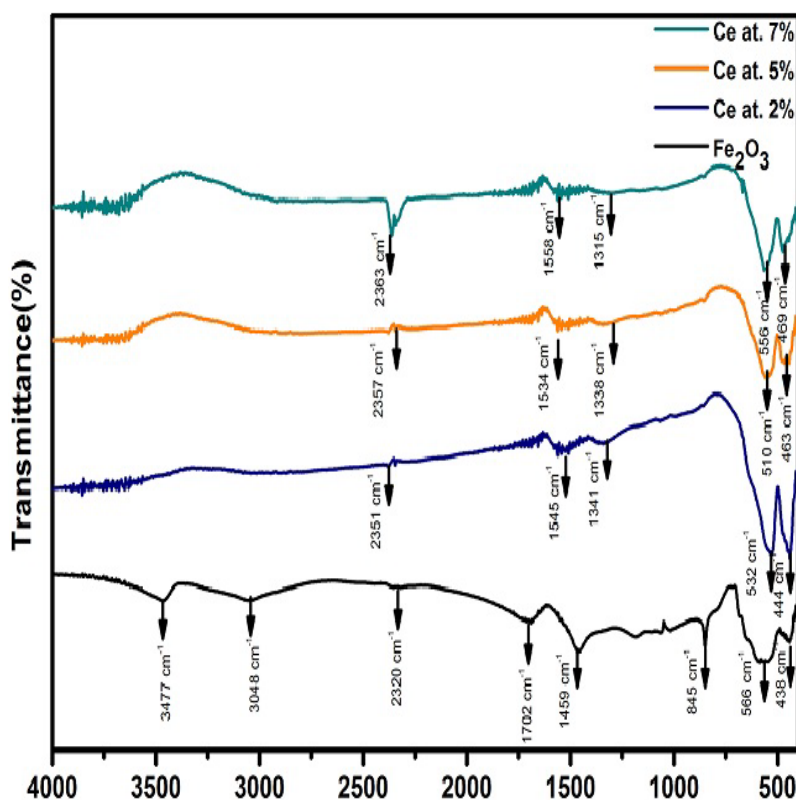


Fig. 6. FTIR spectra of the functional groups for pure  $\text{Fe}_2\text{O}_3$ , Ce doped  $\text{Fe}_2\text{O}_3$  nanostructure.

The stretching vibration bands at 1341  $\text{cm}^{-1}$  and 1045  $\text{cm}^{-1}$  were absorbed by the Ce powder, whereas the bending vibration bands of the water were not [28]. The infrared absorption band of about 2351  $\text{cm}^{-1}$  was due to  $\text{CO}_2$  absorbed from the atmosphere. The asymmetric stretching and symmetrical vibration bands of Ce-O, respectively, were ascribed to the infrared absorption bands at 1545-1045  $\text{cm}^{-1}$  and 532  $\text{cm}^{-1}$  [29, 30]. A typical infrared absorption band for metal oxides is 400  $\text{cm}^{-1}$ [31]. By forming a mixed oxide solution where  $\text{Fe}^{3+}$  was dispersed in the lattice of  $\text{CeO}_2$ , it was determined that the absorption band at 462 and 560  $\text{cm}^{-1}$  in the  $\text{CeO}_2$ -  $\text{Fe}_2\text{O}_3$  mixed oxide had vanished. The Ce-O-Fe stretching band was attributed to the sharp band at around 590  $\text{cm}^{-1}$  [32]. Also, the results confirm the pure and Ce-doped  $\text{Fe}_2\text{O}_3$  nanoparticles formation.

### 3.5. Photo catalytic studies

To conduct the MB dye solution experiments under visible light, it was necessary to assess the photocatalytic activity and calculate the ideal concentration of the used catalysts. The dye

removal procedure was first carried out for 30 minutes in a dark atmosphere to find the maximal absorptive. The pre-equilibrium adsorption of an organic pollutant on the catalyst surface is often directly related to its photodegradation. This can result from Ce doping altering the physical or chemical characteristics of the catalysts. Plots of the degradation % vs. reaction time for different catalyst loading contents are shown in Fig. 7(a-d). According to Fig. 7(a-d), the photodegradation percentage coincided with the catalysts' adsorption attraction for a catalyst loading of 1 g/L. After 180 minutes of visible irradiation, the degradation% for  $\text{Fe}_2\text{O}_3$  and Ce doped  $\text{Fe}_2\text{O}_3$  respectively reached 81, 63, 66, and 67.

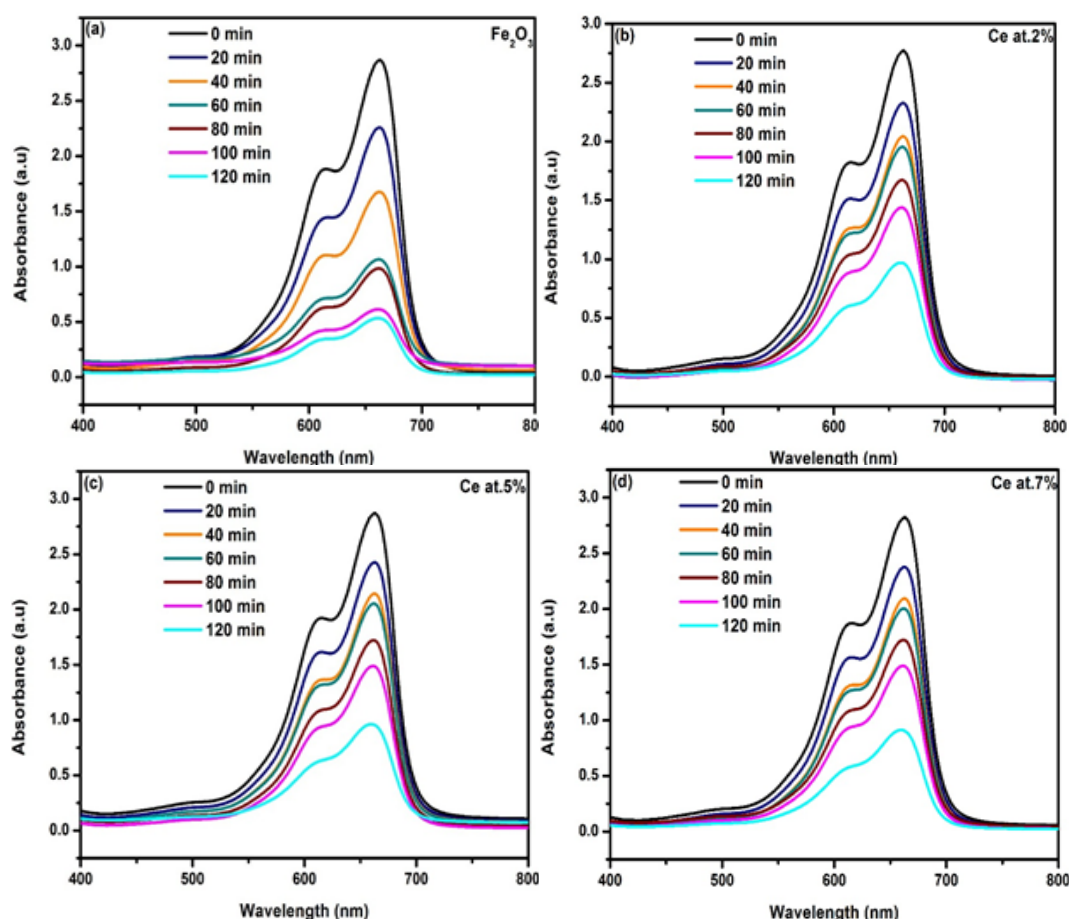


Fig. 7. Absorption spectra of MB solution under visible light irradiation of (a)  $\text{Fe}_2\text{O}_3$  (b) 2% (c) 5% & (d) 7% Ce doped  $\text{Fe}_2\text{O}_3$ .

The lattice parameter shown in Table 1 is mainly related directly to the photoactivity of the produced catalysts. As can be observed, the strength of the MB-corresponding adsorption peak at 662 nm diminished with time in line with the fading of the color. With longer exposure times, the peak maximum of the MB dye's absorbance spectra (at 662 nm) steadily declines, enabling measurement of the dye's photocatalytic discoloration. In this solution color, dark blue was turned into the light blue color of the MB dye solution.

The samples were then examined for degradation performance under irradiation with visible light at 15-minute intervals, as shown in the graph in Fig 7. (a-d). To easily comprehend the photocatalytic performance of the synthesized pure and Ce doped  $\text{Fe}_2\text{O}_3$  samples, it was assumed that MB dye degradation follows first-order kinetics, which can be characterized using the Langmuir-Hinshelwood model as follows (5)

$$\ln(C_0 / C_t) = k_{app}t \quad (5)$$

Where  $k$  is the rate constant, and  $t$  is the reaction time,  $C_0$  and  $C_t$  are the MB initial concentration and at different times  $t$ , respectively [33].

The curves between  $\ln(C_0/C)$  vs irradiation time were plotted to examine the reaction kinetics for this distinct shape of  $Fe_2O_3$  for MB dye degradation (Fig. 7 e, f). It was discovered that Ce-doped  $Fe_2O_3$  samples initially exhibit a rate constant of  $0.00925 \text{ min}^{-1}$ ; however, when the Ce concentration increases to 2%, 5%, and 7%, the rate constant decreases to 0.00821, 0.00936, and  $0.00952 \text{ min}^{-1}$ , respectively, which is 3.5 times less than that of pure  $Fe_2O_3$  samples.

Since the kinetics of MB dye degradation confirmed the pseudo-first-order as stated in Table 2, the produced pure  $Fe_2O_3$  and Ce-doped  $Fe_2O_3$  nanoparticles are the promising materials. It was found that the commercial  $Fe_2O_3$  and Ce doped  $Fe_2O_3$  were exhibited the photodegradation efficiency 81.81, 63.97, 66.68 & 67.73% of MB solution under visible light illumination. However, without the use of a catalyst or exposure to light, MB degradation was not seen. The findings showed that the Ce-doped  $Fe_2O_3$  nanoparticles had photocatalytic activity toward the MB sample solution. Additionally, it was discovered that among this series of Ce-doped  $Fe_2O_3$  photocatalysts, the 2%, 5%, and 7% Ce-doped  $Fe_2O_3$  nanoparticles had the moderate activity. This might be explained by  $Ce^{4+}$  doping, which can give them fascinating features derived from synergetic effects and obviously depending upon the ionic conditions.

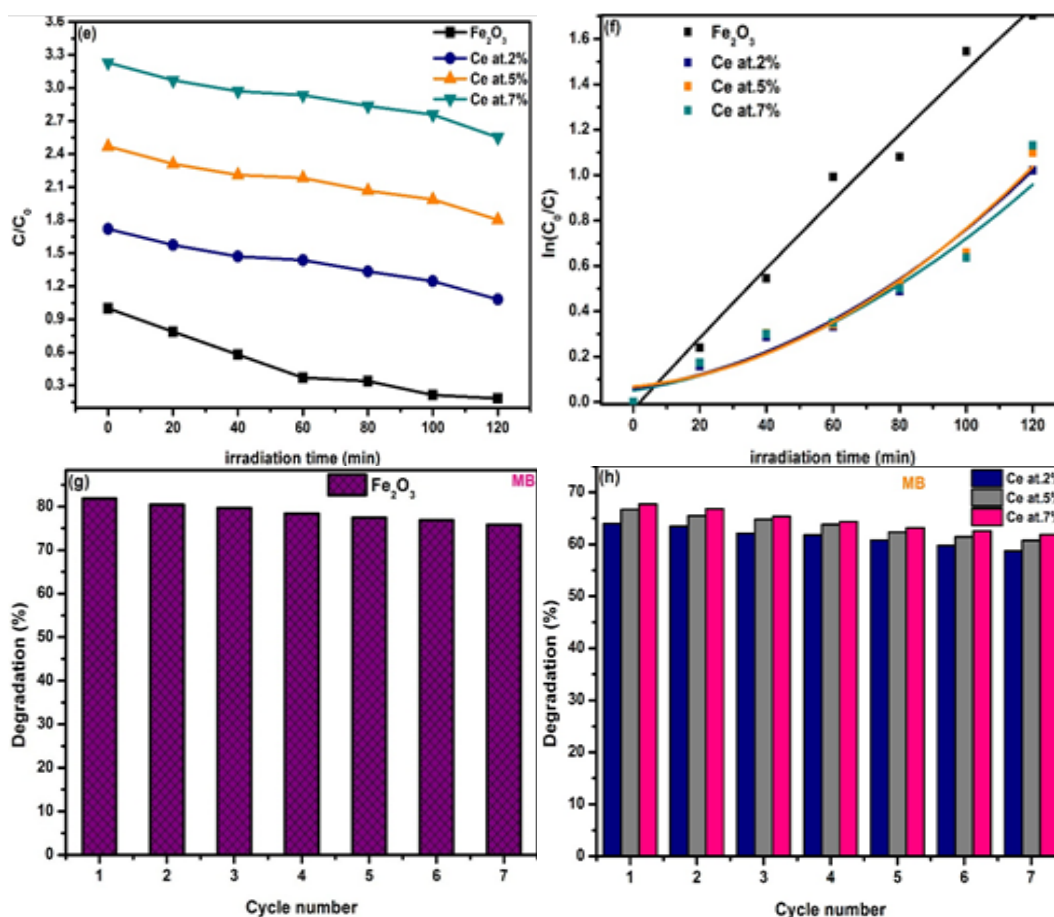


Fig. 7. e)  $C/C_0$  Vs Irradiation time for pure and Ce doped  $Fe_2O_3$  f) Kinetic degradation test of the pure and Ce doped  $Fe_2O_3$  by using MB g) recycling test of MB using Pure  $Fe_2O_3$  and h) recycling test of MB using Ce doped  $Fe_2O_3$  nanostructure.

It can be due to the comparatively high  $\text{Ce}^{4+}$  doping concentration, which may lead to an adsorption of MB to the recombination interior of photogenerated carriers. More hydroxide ions are adsorbed on the ferric surface defects when  $\text{Ce}^{4+}$  ions take the place of  $\text{Fe}^{2+}$  ions. These extra hydroxide ions operate as hole-trapping agents, delaying the electron-hole recombination cycle and photocatalytic activity. Another noteworthy characteristic of  $\text{Ce}^{4+}$  doped  $\text{Fe}_2\text{O}_3$  is the suppression of  $(e^-/h^+)$  recombination and the decrease in visible light absorption. Methylene blue has evident photocatalytic activity using a Ce-doped  $\text{Fe}_2\text{O}_3$  catalyst under visible light illumination. Only 67% of MB was degraded by a Ce-doped  $\text{Fe}_2\text{O}_3$  catalyst, which had the maximum photocatalytic action when exposed to visible light.

Table 2. Stakeout the pseudo-first-order rate constants ( $K$ ),  $R^2$  values, and maximum degradation (%) of the pure and Ce-doped  $\text{Fe}_2\text{O}_3$  nanoparticles.

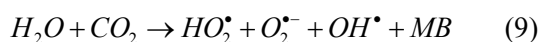
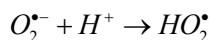
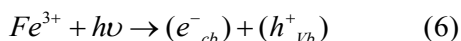
Materials	$K$ (rate constant) $\text{min}^{-1}$	$R^2$	Maximum degradation efficiency (%)
$\text{Fe}_2\text{O}_3$	0.03332	0.9798	81.82
Ce at. 2%	0.02083	0.9543	63.97
Ce at. 5%	0.03056	0.9413	66.68
Ce at. 7%	0.04129	0.9238	67.73

### 3.5.1. Recycle test

We repeated photocatalytic experiments consecutively under experimental circumstances to verify the stability and reusability of Ce-doped  $\text{Fe}_2\text{O}_3$  nanoparticles. Figure 7g-h shows the photo-stability of the Ce-doped  $\text{Fe}_2\text{O}_3$  catalyst; after seven cycles of photodegradation, more than 80% degradation of MB is still accomplished with just a slight fluctuation in photocatalytic performance. These point to adequate stability of Ce-doped  $\text{Fe}_2\text{O}_3$  sample photocatalysts during the photocatalytic process. The loss of some photocatalysts during sample collection by centrifugation and drying for reuse in the photocatalytic experiment may cause the observed drop in the photo degradation rate.

### 3.5.2. Photocatalytic mechanism

From Fig. 8, it can be inferred that both pure and Ce-doped  $\text{Fe}_2\text{O}_3$  nanoparticles exhibit photocatalytic activity for the photodegradation of MB. Based on the excitation of an electron from the valance band (VB) to the conduction band (CB) by the absorption of light of suitable energy, which results in the generation of an equal number of holes in the valance band, the results, a potential photocatalysis mechanism that has the better efficacy of Ce-doped  $\text{Fe}_2\text{O}_3$  nanoparticles, can be explained. The pigment initially adheres to the surface of the  $\text{Fe}_2\text{O}_3$  nanoparticles. An electron ( $e^-$ ) in the VB can be stimulated to the CB with the simultaneous creation of a hole ( $h^+$ ) in the VB when the energy ( $h\nu$ ) of a photon is equal to (or higher) than the bandgap energy of the  $\text{Fe}_2\text{O}_3$  semiconductor materials. Under visible light irradiation, the CB electrons ( $e^-_{\text{cb}}$ ) and VB holes ( $h^+_{\text{vb}}$ ) are generated in the presence of an aqueous  $\text{Fe}_2\text{O}_3$  nanocomposite suspension. Surface  $\text{Fe}^{3+}$  ions operate as an electron acceptor or hole donor, allowing charge carriers to localize and hence extend separation by trapping at energy levels in the conduction or valance bands [34-35]. In general, the photocatalysis mediated by pure and Ce-doped  $\text{Fe}_2\text{O}_3$  can be explained as follows. When an MB dye solution containing the  $\text{Fe}_2\text{O}_3$  is exposed with light energy more significant than its band gap energy, the electron in the VB of  $\text{Fe}_2\text{O}_3$  jumps to the CB ( $e^-_{\text{cb}}$ ), leaving behind holes ( $h^+_{\text{vb}}$ ) in the VB. Additionally,  $\text{O}_2$  that has been dissolved in water or adsorbed on the surface of a nanocomposite can react with the photogenerated electrons ( $e^-_{\text{cb}}$ ) to form superoxide radical anion  $\text{O}_2^-$ . The photogenerated holes ( $h^+_{\text{vb}}$ ) can interact with OH or  $\text{H}_2\text{O}$  and become OH radicals. According to equations (6-9), the following high oxidant species hydroxyl radical (OH), peroxide radicals ( $\text{HO}_2$ ), and superoxide radical anion  $\text{O}_2^-$  are claimed to be responsible for the photodecomposition of MB dye.



The three used catalysts' photodegradation rates increased when the catalyst loading was raised to 2 g/L. Typically, when catalyst concentration increases, more active sites appear on the photocatalyst surface, which leads to an increase in the production of OH radicals [37-39].

The better degradation efficiency of the MB dye of Ce-doped  $Fe_2O_3$  composite is adsorption affinity, reaching the maximum under 2 g/L of catalyst loading. Thus, 63% out of the 67% efficiency attained under visible light irradiation was due to MB dye. Thus, the efficiency is adsorption shows that sample Ce at 7% is shown at 67%, so cerium increasing also efficiency will be increased are regularly irradiation due to the increase of the electron trapping capability of  $Ce^{4+}$  ions, Lewis acid [40]. The electrons are transferred to surrounding adsorbed  $O_2$  by the oxidation process attentive, so the CeO alerts the  $e^+/h^-$  recombination rate through the subsequent process condition [41]

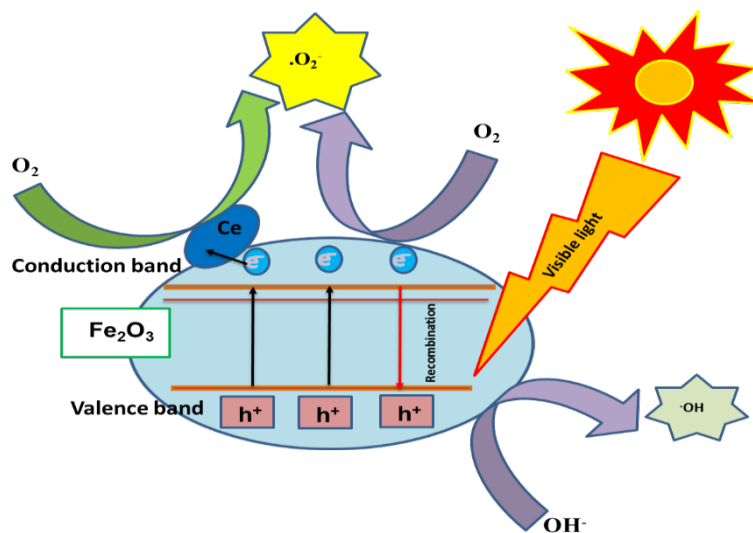
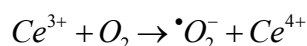
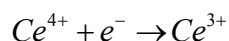


Fig. 8. Schematic representation for the photocatalytic mechanism of pure and Ce doped  $Fe_2O_3$  catalyst under visible light irradiation.

$Fe_2O_3$  and Ce-doped  $Fe_2O_3$  samples were used as an example to find and separate the intermediate produced during the photodegradation of the MB dye to verify the photocatalytic activity of the developed catalysts. Moreover, beyond Ce-doped  $Fe_2O_3$  loading, the solution turns turbid and scatters light radiation, which makes it difficult for the reaction to advance. As a result, the degradation percentage decreases [42].

#### 4. Conclusion

In summary, pure and Ce-doped Fe<sub>2</sub>O<sub>3</sub> NPs were successfully prepared through a sol-gel technique. The hexagonal phase transition of the Fe<sub>2</sub>O<sub>3</sub> and Ce. 2, 5 & 7% doped Fe<sub>2</sub>O<sub>3</sub> NPs were determined from XRD analysis. The morphological analysis confirmed that nanorods with nanosphere-like structures. Additionally, the TEM analysis confirms the nanorod-like structure, and the SAED pattern along the direction plane [018] with 0.21 nm lattice d-spacing growth further confirms the formation of the materials. Functional groups are found from products predicted from the FT-IR analysis. From the photocatalytic activity, the prepared pure and Ce doped Fe<sub>2</sub>O<sub>3</sub> nanostructures have photocatalytic behaviour in the UV light environment. Incorporating Ce<sup>4+</sup> ions into the Fe<sub>2</sub>O<sub>3</sub> matrix introduces new defect levels, which can act as trap centers and thereby minimize the recombination rate by effectively separating electron-hole (e<sup>-</sup>/h<sup>+</sup>) pairs.

#### References

- [1] F. Marye Anne, J. Org. Chem. 74 (22), 8497 (2009); <https://doi.org/10.1021/jo901731t>
- [2] F. Aslani, S. Bagheri, N. M. Julkapli, Growth: An Overview. Sci. World J. 641759 (2014); <https://doi.org/10.1155/2014/641759>
- [3] V. I. Alexiadis, N. Boukos, X. E. Verykios, Mater, Chem. Phys. 128, 96 (2011); <https://doi.org/10.1016/j.matchemphys.2011.02.075>
- [4] M. Mishra, D.M. Chun, Appl. Catal. A 498, 126 (2015); <https://doi.org/10.1016/j.apcata.2015.03.023>
- [5] S. Li, S. Hu, J. Zhang, W. Jiang, J. Liu, J. Colloid Interface. Sci. 497, 93 (2017); <https://doi.org/10.1016/j.jcis.2017.02.069>
- [6] D. Kubaniova, P. Brazda, K. Zaveta, T. Kmjec, M. Klementova, J. Kohout, Journal of Magnetism and Magnetic Materials 472(15), 96 (2019)
- [7] J. YuanZhao, N. Ren, J. Jun Zhang, Polyhedron 15, 114892 (2021)
- [8] K. Sekizawa, S. Sato, T. Arai, T. Morikawa, ACS Catal. 8 (2), 1405 (2018); <https://doi.org/10.1021/acscatal.7b03244>
- [9] R.G. Marques, A.M.F. Lima, V.S. Santana, N.R.C.F. Machado, J. Environ. Manage. 195, 242 (2017); <https://doi.org/10.1016/j.jenvman.2016.08.034>
- [10] S.K. Md Saad, A.A. Umar, M.I.A. Umar, M. Tomitori, M.Y.A. Rahman, M.M. Salleh, M. Oyama, ACS Omega 3(3), 2579 (2018); <https://doi.org/10.1021/acsomega.8b00109>
- [11] C.B.D. Marien, T. Cottineau, D. Robert, P. Drogui, Appl. Catal. B: Environ. 194, 1 (2016); <https://doi.org/10.1016/j.apcatb.2016.04.040>
- [12] Z. Wang, G. Zou, W. Wang, Z. Tang, Y. Bi, X. Wang, J. Power Sources 343, 94 (2017); <https://doi.org/10.1016/j.jpowsour.2017.01.035>
- [13] S.W. Bennett, A.A. Keller, Appl. Catal. B: Environ. 102, 600 (2011); <https://doi.org/10.1016/j.apcatb.2010.12.045>
- [14] S. Phanichphant, A. Nakaruk, D. Channei, Appl. Surf. Sci. 387, 214 (2016); <https://doi.org/10.1016/j.apsusc.2016.06.072>
- [15] O. Lupan, V. Postica, J. Grottrup, A.K. Mishra, N.H. de Leeuw, R. Adelung, Sens. Actuat. B: Chem. 245, 448 (2017); <https://doi.org/10.1016/j.snb.2017.01.107>
- [16] F. Arena, B. Gumina, A.F. Lombardo, C. Espro, A. Patti, L. Spadaro, L. Spiccia, Appl. Catal. B: Environ. 162, 260 (2015); <https://doi.org/10.1016/j.apcatb.2014.06.054>
- [17] F. Ke, L. Qiu, J. Zhu, Nanoscale 6, 1596 (2014); <https://doi.org/10.1039/C3NR05051C>
- [18] G.K. Pradhan, K.H. Reddy, K.M. Parida, Catal. Today 224, 171 (2014); <https://doi.org/10.1016/j.cattod.2013.10.038>
- [19] S. Fang, Y. Xin, L. Ge, C. Han, P. Qiu, L. Wu, Appl. Catal. B: Environ. 179, 458 (2015); <https://doi.org/10.1016/j.apcatb.2015.05.051>

- [20] M. Faisal, M. Abu Tariq, M. Muneer, *Dyes Pigment.* 72, 233 (2007); <https://doi.org/10.1016/j.dyepig.2005.08.020>
- [21] A.A. Ismail, D.W. Bahnemann, *Green Chem.* 13, 428 (2011); <https://doi.org/10.1039/c0gc00744g>
- [22] T.Y. Ma, Z.Y. Yuan, J.L. Cao, *Eur. J. Inorg. Chem.* 5, 716 (2010); <https://doi.org/10.1002/ejic.200900991>
- [23] H. Kiziltaş, T. Tekin, D. Tekin, *Jour. Envir. Chemi. Engin.* 8(5), 104160 (2020); <https://doi.org/10.1016/j.jece.2020.104160>
- [24] X. Liu, J. Zhang, S. Wu, D. Yang, P. Liu, H. Zhang, S. Wang, X. Yao, G. Zhu, H. Zhao, *RSC Adv.* 2, 6178 (2012); <https://doi.org/10.1039/c2ra20797d>
- [25] R. Pena-Garcia, Y. Guerra, B. V. M. Farias, F. E. P. Santos, F. X. Nobre, J. P. Caland, H. S. V. Pessoni, A. Franco, Jr, E. Padron-Hernández, *Ceram. Int.* 45, 918 (2019); <https://doi.org/10.1016/j.ceramint.2018.09.267>
- [26] S. Li, K. Yao, L. Fu, M. Ma, *RSC Adv* 6, 2135 (2016); <https://doi.org/10.1039/C6RA04551K>
- [27] S. Basavaraja, D.S. Balaji, M.D. Bedre, D. Raghunandan, S. Prithviraj, A. Venkataraman, *Bull. Mater. Sci.* 34, 1313 (2012); <https://doi.org/10.1007/s12034-011-0321-z>
- [28] Y. P. Fu, C.H. Lin, C. S. Hsu, *J. Alloys Compd.* 391, 110 (2005); <https://doi.org/10.1016/j.jallcom.2004.07.079>
- [29] J. Baneshi, M. Haghghi, N. Jodeiri, *Energy Convers. Manag.* 87, 928 (2014); <https://doi.org/10.1016/j.enconman.2014.07.058>
- [30] S.B. Khan, M. Faisal, M.M. Rahman, *Sci. Total Environ.* 409, 2987 (2011); <https://doi.org/10.1016/j.scitotenv.2011.04.019>
- [31] A. Saberi, F. Golestani-Fard, H. Sarpoolaky, *J. Alloys Compd.* 462, 142 (2008); <https://doi.org/10.1016/j.jallcom.2007.07.101>
- [32] S.B. Khan, M. Faisal, M. M. Rahman, A. Jamal, *Int. J. Electro. Chem. Sci.* 8, 7284e97 (2013)
- [33] M. Faisal, Adel A. Ismail, Ahmed A. Ibrahim, Houcine Bouzid, Saleh A. Al-Sayari, *Chem. Eng. J.* 229, 225 (2013); <https://doi.org/10.1016/j.cej.2013.06.004>
- [34] T. Masui, H. Hirai, N. Imanaka, *J. Mater. Sci. Lett.* 21, 489 (2002); <https://doi.org/10.1023/A:1015342925372>
- [35] R.A. Elsalamony, *Res. Rev.: J. Mater. Sci.* 4(2), 26 (2016)
- [36] K. Azad, P. Gajanan, *Chem. Sci. J.* 8, 164 (2017)
- [37] R. A. Elsalamony, S.A. Mahmoud, *Arab. J. Chem.* 10, 194 (2017); <https://doi.org/10.1016/j.arabjc.2012.06.008>
- [38] X. H. Zhang, Y. L. Zhuang, W. Sun, X. J. Li, L. W. Shan, L. M. Dong, *Dig. J. Nanomater. Biostructures.* 15, 1025 (2020)
- [39] T. Rungsawang, S. Sujinnapram, S. Nilphai, S. Wongrerkerdee, *Dig. J. Nanomater. Biostructures.* 16, 1209 (2021)
- [40] J.M. Coronado, A.J. Maira, A. Martanez-Arias, J.C. Conesa, J. Soria, *J. Photochem. Photobiol. A Chem.* 150, 213 (2002); [https://doi.org/10.1016/S1010-6030\(02\)00092-8](https://doi.org/10.1016/S1010-6030(02)00092-8)
- [41] Y. Xie, C. Yuan, *Appl. Catal. B Environ.* 46, 251 (2003); [https://doi.org/10.1016/S0926-3373\(03\)00211-X](https://doi.org/10.1016/S0926-3373(03)00211-X)
- [42] H.M. Coleman, V. Vimonses, G. Leslie, R. Amal, *J. Hazard Mater.* 146, 496 (2007); <https://doi.org/10.1016/j.jhazmat.2007.04.049>